Lattice-gas cellular-automaton method for semiclassical transport in semiconductors

K. Kometer, G. Zandler, and P. Vogl
Physik Department and Walter Schottky Institut, Technische Universität München, D-8046 Garching, Federal Republic of Germany
(Received 3 February 1992)

A cellular-automaton method for solving the Boltzmann equation for semiclassical transport is presented and applied to nonlinear transport in semiconductors. It is shown that the Boltzmann equation for semiconductor transport can be transformed into a Boolean master equation, which represents a cellular automaton with nearest-neighbor interaction in position space. The resulting numerical algorithm is physically equivalent to the ensemble Monte Carlo method and tailored to modern vector or parallel processing. The algorithm is well suited for carrier systems with pronounced spatial inhomogeneities, large density variations, and scattering kernels involving single- and more-particle interactions. Several tests of the cellular-automaton technique for nonlinear transport in Si and GaAs are presented. The results agree very well with published Monte Carlo calculations.

I. INTRODUCTION

Recently, an effective simulation strategy has been developed for the realistic modeling of transport processes in a variety of problems. The physical systems are replaced by fictitious microworld models obeying discrete cellular-automaton rules such that the macroscopic dynamics is recovered as an ensemble average over the microworld states.[1,2] In hydrodynamics, for example, Frisch and co-workers[3,4] could show that lattice-gas automata can provide an effective numerical technique for solving the Navier-Stokes and many other types of partial differential equations with complex boundary conditions. In the study of chemical reactions,[5,6] or nonequilibrium growth,[7] cellular-automaton models have also been found to provide additional microscopic insights into the complex behavior of nonlinear dynamical systems, particularly concerning the relation between global dynamics and local physical laws.

The concept of cellular automata (CA) goes back to von Neumann.[8] A cellular automaton is a discrete dynamical system which evolves in discrete time steps. It is defined at the nodes of a lattice, each site of which is characterized by a finite number of Boolean states. In the context of transport theory, these Boolean states are classified as being occupied or empty, and the former ones are considered as representing fictitious "particles." In each time step, a set of transition rules updates the state occupancies synchronously on all lattice sites. The important point is that these rules are local in the sense that they only act on the occupancies of a given site and its nearest (and possibly second-nearest) neighbors. It is precisely for this reason that the CA constitutes one of the very few algorithms for dynamical systems that can optimally utilize massively parallel processor hardware.[1,2] In addition, the locality of the dynamical rules allows an efficient and flexible handling of complex geometries and lattice topologies. A noticeable recent example is a CA simulation of flow through porous media with a fractal structure.[9] Furthermore, the exclusive usage of Boolean variables implies that the state function of the physical system can be characterized in a highly compact way and with numerical precision that can be optimally adapted to each individual physical observable. Finally, the reduction to logics causes this technique to be free of round-off noise.

There are two crucial factors that set cellular automata apart from standard finite-difference methods for partial-differential equations. First, Frisch, Hasslacher, and Pomeau[3] demonstrated in their fundamental paper on lattice-gas automata for fluid dynamics that one can construct a set of extremely simple microscopic Boolean evolution rules that asymptotically yield the Euler or Navier-Stokes equations by macroscopic averaging. This work, which has subsequently been extended and refined in various ways,[1] suggests that it is possible to replace highly nonlinear partial differential equations—possessing singular or chaotic solutions—with a large set of individually trivial problems that involve only logical and, therefore, numerically stable operations and can be solved in parallel. This is one reason for the numerical efficiency of CA.

The second basic property of CA is the reduction of all physical variables to Boolean values. Microscopic transport equations contain scattering kernels that depend on many physical parameters. Often, the solution is insensitive to some of these parameters and it is unnecessary to store them with high precision. In low-speed diffusive transport regimes, for example, the detailed angular dependence of a particle-particle collision rate is irrelevant. By representing each parameter by only as many bits as necessary and treating them on an equal footing, lattice-gas automata can achieve substantial reductions in storage requirements, as will be elaborated in later sections of this paper.

The field of CA has not sufficiently matured yet to allow a final judgment of this method. The following limitations of CA, however, are generally relevant and are the focus of much of the ongoing research.[1,2] First of all, CA simulations require choosing a finite precision for all variables, which is, strictly speaking, possible only *a posteriori*. In the published applications we are aware of, ac-

ceptable bounds could be taken *a priori* for the relevant variables (e.g., particle velocity or energy) on physical grounds. Second, the dynamics on a discrete lattice lacks Galilean invariance and full rotational symmetry. Often, this fact may not be relevant but it affects CA simulations of fluid dynamics for high Reynolds numbers very unfavorably due to the mutual interaction of turbulent patterns of all length scales. Third, most realistic lattice-gas simulations employ nondeterministic rules. These rules can lead to artificial dispersion effects that hamper the simulation of coherent wave motion extending over many wavelengths or highly ballistic motion which is characteristic of quantum transport. Interesting solutions to these problems have been proposed recently.[10–13] Even if the cellular-automaton method turns out to be less useful for highly turbulent flow or phase-coherent motion, there is still a wide area of semiclassical transport problems in plasma physics, astrophysics, and particularly semiconductor physics where the drift by external forces and diffusion due to density variations are equally relevant and turbulence phenomena play no role.

In this paper, we demonstrate that CA simulations offer some striking advantages in the area of semiclassical Boltzmann transport for charged or neutral plasmas, i.e., for integro-differential equations in situations with pronounced spatial inhomogeneities, large density variations, and scattering kernels involving single- and more-particle interactions. As a concrete application, we focus on nonlinear transport in semiconductors.

The central result of this paper is that the nonlocal Boltzmann equation in $(6+1)$-dimensional $(\mathbf{x},\mathbf{k};t)$ phase space for carrier transport in solids can be transformed to a Boolean master equation, which constitutes a lattice-gas automaton with nearest-neighbor interactions in position space and stochastic rules. This transformation effectively decouples $\mathbf{x}$ and $\mathbf{k}$ space. The CA rules can be systematically calculated from the quantum-mechanical scattering rates and the equations of motion for the Bloch states. In this way we obtain a simulation technique for nonlinear semiconductor transport which is comparable in accuracy to the standard ensemble Monte Carlo simulations, and is tailored to modern vector or parallel computer hardware. The transformation to Boolean variables and local interactions in real space allows one to deal efficiently with arbitrarily complex spatial inhomogeneities, large variations in carrier density, and carrier-carrier collisions with only minimal additional costs in computer time.

The vast majority of semiconductor high-field transport calculations that deal with the full $(\mathbf{x},\mathbf{k};t)$ phase space for the Boltzmann distribution function are based on the ensemble Monte Carlo technique[14] (for a survey and discussion of the method, see Refs. 15 and 16). The presently developed lattice-gas method is an alternative approach to reaching the same goal, namely to solve the Boltzmann equation quantitatively. In both methods, the Boltzmann equation is reduced to stochastic-rate equations. In the Monte Carlo approach, however, these are augmented by the semiclassical equations of motion. In contrast, the CA master equations incorporate the equations of motion into the collisions processes, which greatly simplifies the solution of the CA equations. The actual CA simulations solely map Boolean arrays onto one another.

In Sec. II, the Boltzmann equation for semiconductors is mapped onto a nearest-neighbor cellular automaton. In Sec. III, generic numerical algorithms for CA simulations of the Boltzmann equation are discussed. Concrete tests and comparisons to ensemble Monte Carlo results are given in Sec. IV. In these examples, the spatial anisotropy is confined to two dimensions, whereas the momentum space is included three-dimensionally albeit in a simplified form. Even for this rather crude discretization of phase space, we find that the presently developed CA is already comparable in accuracy to standard Monte Carlo calculations. Finally, in Sec. V we investigate velocity overshoot in a Si device as an application of the CA technique. We note that we have previously published a short paper about this method with some additional results.[17]

II. THEORY

In this section a cellular automaton is developed that yields the semiclassical Boltzmann equation in the limit of an ensemble average over the cellular automaton states. This automaton has the following general properties. It is defined on the sites of a lattice in real space $\mathbf{x}$, and attached to each site $\mathbf{x}$ there is a set of momentum states which we term $\mathbf{k}$ cells. These $\mathbf{x}$ sites and $\mathbf{k}$ cells are populated by fictitious particles—the lattice-gas particles—which obey nondeterministic dynamical rules. These automaton rules consist of (i) transitions between any of the $\mathbf{k}$ cells on the same site $\mathbf{x}$ and (ii) transitions between *corresponding* $\mathbf{k}$ cells on neighboring lattice sites. The rules themselves, i.e., the probabilities for these transitions, are determined by the quantum-mechanical scattering mechanisms and the classical equations of motion. The physical trajectories and macroscopic observables are obtained by averaging over many phase-space automaton cells.

In hydrodynamics, the usual starting point for the development of CA models is a set of microscopic rules. Then, the major task consists in deriving the corresponding macroscopic equations by an appropriate Chapman-Enskog expansion.[1–3] In the present work, the inverse procedure is followed instead. We start from the continuous semiclassical Boltzmann equation and *derive* the rules for a cellular automaton. The central step in this derivation is the replacement of the kinematic terms in the Boltzmann equation by effective scattering probabilities that yield the macroscopic equations of motion in the ensemble average.

The Boltzmann equation for the single-particle distribution function $f(\mathbf{x},\mathbf{k};t)$ can be written in the form

$$\left.\frac{\partial f}{\partial t}+\frac{\partial f}{\partial t}\right|_F=\left.\frac{\partial f}{\partial t}\right|_{\text{coll}}. \tag{2.1}$$

The collision term contains the total quantum-mechanical scattering probability per unit time due to elastic and inelastic processes. To elucidate the basic principles of the present scheme and keep the equations transparent, we restrict ourselves to nondegenerate elec-

trons in a single band in this section. We note, however, that degeneracy and multiband effects can be included very efficiently in the lattice-gas method. With these restrictions, the collision term has the form

$$\left.\frac{\partial f}{\partial t}\right|_{\text{coll}}=\frac{V}{(2\pi)^3}\int d\mathbf{k}'\{w(\mathbf{x},\mathbf{k}',\mathbf{k})f(\mathbf{x},\mathbf{k}';t) -w(\mathbf{x},\mathbf{k},\mathbf{k}')f(\mathbf{x},\mathbf{k};t)\} . \tag{2.2}$$

In these equations, V is the crystal volume and $w(\mathbf{x},\mathbf{k}',\mathbf{k})$ the scattering probability per unit time from Bloch state $\mathbf{k}'$ into state $\mathbf{k}$. In the form of Eq. (2.2), the collision term is sufficiently general to allow the inclusion of all types of elastic and inelastic one-particle scattering mechanisms such as phonons, impurities, disorder, and boundaries. The crucial point is that the collision term Eq. (2.2) is local in position space. This locality is a basic assumption underlying the Boltzmann equation and remains valid even when two-particle Coulomb scattering is included. In contrast, the change in the distribution function due to applied fields,

$$\left.\frac{\partial f}{\partial t}\right|_{F}=\dot{\mathbf{x}}\cdot\nabla_x f(\mathbf{x},\mathbf{k};t)+\dot{\mathbf{k}}\cdot\nabla_k f(\mathbf{x},\mathbf{k};t) , \tag{2.3}$$

supplemented by the equations of motion for Bloch wave packets of momentum $\mathbf{k}$, charge $-e$, and energy dispersion $\varepsilon(\mathbf{k})$,

$$\dot{\mathbf{x}}=\frac{1}{\hbar}\nabla_k\varepsilon(\mathbf{k}) , \qquad \dot{\mathbf{k}}=-\frac{e}{\hbar}\mathbf{E}(\mathbf{x}) , \tag{2.4}$$

is nonlocal in both position and momentum space. Consequently, one major obstacle in converting the Boltzmann equation to *a local* CA is not the collision term, Eq. (2.2), but the explicit nonlocality of Eqs. (2.3) and (2.4) which link the distribution function $f(\mathbf{x},\mathbf{k};t)$ to its value in different $(\mathbf{x}',\mathbf{k}')$ locations. An additional obstacle is the different functional forms of Eqs. (2.2) and (2.3). Whereas a discretized version of Eq. (2.2) has the form of a master equation and can easily be envisaged as a transition of a lattice-gas particle from one state to another with probability w, Eq. (2.3) does not suggest a similar interpretation. In this section we show that Eq. (2.3) can be transformed to an *effective* collision term of the same type as Eq. (2.2), which is also local in $\mathbf{x}$ space.

The first step in converting the Boltzmann equation to an automaton consists in discretizing the Boltzmann equation with respect to time, position, and Bloch momentum. The time derivatives in the above equations are replaced by finite differences with small time steps Δt. Additionally, we define lattices in real and momentum space, with the cells being labeled by indices $\mathbf{R}$ and $\mathbf{K}$, respectively, so that

$$\mathbf{x}=\mathbf{R}+\mathbf{r} , \qquad \mathbf{k}=\mathbf{K}+\mathbf{q} , \tag{2.5}$$

where $\mathbf{R}$ and $\mathbf{K}$ denote the cell centers and $\mathbf{r}$ and $\mathbf{q}$ vary within the cells. The cell volumes are denoted by $V(\mathbf{R})$ and $V(\mathbf{K})$, respectively. Since the total phase space is the product of real and momentum space, one has to attach the complete $\mathbf{K}$ lattice to each site in $\mathbf{R}$ space. In the discretization scheme we have adopted, the $\mathbf{K}$ lattice attached to site $\mathbf{R}$ is constructed in spherical polar coordinates around $\mathbf{R}$. Each $\mathbf{K}$ vector points toward one of the nearest (and, in general, more distant) neighbors in $\mathbf{R}$ space.

By replacing all derivatives in Eqs. (2.1)–(2.3) by finite differences, one obtains

$$f(\mathbf{x},\mathbf{k};t+\Delta t)=f(\mathbf{x},\mathbf{k};t)+|\dot{\mathbf{x}}|\frac{\Delta_x f}{\Delta x}\Delta t +|\dot{\mathbf{k}}|\frac{\Delta_k f}{\Delta k}\Delta t+\left.\frac{\partial f}{\partial t}\right|_{\text{coll}}\Delta t , \tag{2.6}$$

$$\Delta_x f(\mathbf{x},\mathbf{k};t)=f(\mathbf{x}-\Delta\mathbf{x},\mathbf{k};t)-f(\mathbf{x},\mathbf{k};t) , \tag{2.7}$$

$$\Delta_k f(\mathbf{x},\mathbf{k};t)=f(\mathbf{x},\mathbf{k}-\Delta\mathbf{k};t)-f(\mathbf{x},\mathbf{k};t) . \tag{2.8}$$

In these equations, we have defined the difference vectors $\Delta\mathbf{x}=(\Delta x)\dot{\mathbf{x}}/|\dot{\mathbf{x}}|$, and $\Delta\mathbf{k}=(\Delta k)\dot{\mathbf{k}}/|\dot{\mathbf{k}}|$. Note that $\Delta\mathbf{x}$ and $\Delta\mathbf{k}$ are coupled with one another by the equations of motion, Eq. (2.4). By using Eq. (2.4) and by defining the time $t_x(v)$ required for an electron with velocity $\mathbf{v}=\dot{\mathbf{x}}$ to move over a distance $\Delta\mathbf{x}$,

$$t_{\Delta x}(v)=\frac{\Delta x}{|\dot{\mathbf{x}}|} , \tag{2.9}$$

we can write Eq. (2.6) as

$$f(\mathbf{x},\mathbf{k};t+\Delta t)=f(\mathbf{x},\mathbf{k};t)+\frac{\Delta t}{t_{\Delta x}(v)}\Delta_x f(\mathbf{x},\mathbf{k};t) +\frac{e|\mathbf{E}(\mathbf{x})|\Delta t}{\hbar\Delta k}\Delta_k f(\mathbf{x},\mathbf{k};t) +\left.\frac{\partial f}{\partial t}\right|_{\text{coll}}\Delta t . \tag{2.10}$$

Next, the distribution function $f(\mathbf{x},\mathbf{k};t)$ is replaced by a cell-integrated occupancy in the phase-space cell $(\mathbf{R},\mathbf{K})$,

$$N(\mathbf{R},\mathbf{K};t)=\int_{V(\mathbf{R})}d\mathbf{x}\int_{V(\mathbf{K})}\frac{d\mathbf{k}}{(2\pi)^3}f(\mathbf{x},\mathbf{k};t) . \tag{2.11}$$

We assume that the cells in phase space are sufficiently small so that $f(\mathbf{x},\mathbf{k};t)$ can be replaced by its cell average and obtain

$$N(\mathbf{R},\mathbf{K};t)=\frac{1}{(2\pi)^3}V(\mathbf{R})V(\mathbf{K})f(\mathbf{R},\mathbf{K};t) . \tag{2.12}$$

When the Boltzmann equation is integrated over one phase-space cell $(\mathbf{R},\mathbf{K})$, it reads

$$N(\mathbf{R},\mathbf{K};t+\Delta t)=N(\mathbf{R},\mathbf{K};t)+\Delta N(\mathbf{R},\mathbf{K};t)_T +\Delta N(\mathbf{R},\mathbf{K};t)_E+\Delta N(\mathbf{R},\mathbf{K};t)_{\text{coll}} . \tag{2.13}$$

The four terms on the right-hand side of Eq. (2.13) exactly correspond to those in Eq. (2.10). The indices T and E label the translation- and electric-field-induced terms, respectively. By forming cell averages in Eq. (2.2), the collision term can be expressed in terms of the cell-integrated occupancies,

$$\Delta N(\mathbf{R},\mathbf{K};t)_{\text{coll}}=\int_{V(\mathbf{R})}d\mathbf{x}\int_{V(\mathbf{K})}\frac{d\mathbf{k}}{(2\pi)^3}\frac{V}{(2\pi)^3}\int d\mathbf{k}'\{w(\mathbf{x},\mathbf{k}',\mathbf{k})f(\mathbf{x},\mathbf{k}';t)-w(\mathbf{x},\mathbf{k},\mathbf{k}')f(\mathbf{x},\mathbf{k};t)\}\Delta t$$
$$=\sum_{\mathbf{K}'}\int_{V(\mathbf{R})}d\mathbf{x}\int_{V(\mathbf{K})}\frac{d\mathbf{k}}{(2\pi)^3}V\int_{V(\mathbf{K}')}\frac{d\mathbf{k}'}{(2\pi)^3}\{w(\mathbf{x},\mathbf{k}',\mathbf{k})f(\mathbf{x},\mathbf{k}';t)-w(\mathbf{x},\mathbf{k},\mathbf{k}')f(\mathbf{x},\mathbf{k};t)\}\Delta t$$
$$=\sum_{\mathbf{K}'}\{P_{\text{coll}}(\mathbf{R},\mathbf{K}',\mathbf{K})N(\mathbf{R},\mathbf{K}';t)-P_{\text{coll}}(\mathbf{R},\mathbf{K},\mathbf{K}')N(\mathbf{R},\mathbf{K};t)\}\ . \tag{2.14}$$

In this equation, we have introduced the integrated transition probabilities between cells $\mathbf{K}$ and $\mathbf{K}'$,

$$P_{\text{coll}}(\mathbf{R},\mathbf{K}',\mathbf{K})=\frac{V}{V(\mathbf{R})V(\mathbf{K}')}\int_{V(\mathbf{R})}d\mathbf{x}\int_{V(\mathbf{K})}d\mathbf{k}\int_{V(\mathbf{K}')}\frac{d\mathbf{k}'}{(2\pi)^3}w(\mathbf{x},\mathbf{k}',\mathbf{k})\Delta t\ . \tag{2.15}$$

In order for P_{coll} to represent a probability, the time step Δt must be chosen sufficiently short so that the equation

$$\sum_{\mathbf{K}}P_{\text{coll}}(\mathbf{R},\mathbf{K}',\mathbf{K})\le 1 \tag{2.16}$$

is obeyed for all $\mathbf{K}'$. In the Appendix, the calculation of this cell-averaged collision rate P_{coll} is exemplified for optical phonons.

In the next and crucial step, we convert the other contributions in Eq. (2.13) to a form which is identical to Eq. (2.14), with P_{coll} being replaced by some effective transition probabilities. To this end, we introduce the quantity

$$\Delta_k N(\mathbf{R},\mathbf{K};t)=\left[\frac{e|\mathbf{E}(\mathbf{R})|\Delta t}{\hbar\Delta k}\right]^{-1}\Delta N(\mathbf{R},\mathbf{K};t)_E\ , \tag{2.17}$$

and the local distribution function

$$f_{\mathbf{RK}}(\mathbf{x},\mathbf{k};t)=\begin{cases}f(\mathbf{R},\mathbf{K};t), & \mathbf{x}\in V(\mathbf{R})\text{ and }\mathbf{k}\in V(\mathbf{K})\\ 0\ \text{ otherwise}\ .\end{cases} \tag{2.18}$$

With Eqs. (2.10) and (2.13), one obtains

$$\Delta_k N(\mathbf{R},\mathbf{K};t)=\sum_{\mathbf{R}',\mathbf{K}'}\int_{V(\mathbf{R})}d\mathbf{x}\int_{V(\mathbf{K})}\frac{d\mathbf{k}}{(2\pi)^3}\times f_{\mathbf{R}'\mathbf{K}'}(\mathbf{x},\mathbf{k}-\Delta\mathbf{k};t)$$
$$-N(\mathbf{R},\mathbf{K};t)\ . \tag{2.19}$$

Since the shifted $\mathbf{k}$ vector in the argument of $f_{\mathbf{R}'\mathbf{K}'}$ is not centered in any cell $\mathbf{k}$, i.e., $\mathbf{K}-\Delta\mathbf{k}\neq\mathbf{K}'$, the integral in Eq. (2.19) cannot be expressed in terms of the cell-integrated occupancy $N(\mathbf{R}',\mathbf{K}';t)$ immediately. In order to achieve this, we rigidly shift the whole cell centered at wave vector $\mathbf{K}$ by an amount $-\Delta\mathbf{k}$. The integral on the right-hand side of Eq. (2.19) is then proportional to the geometrical overlap in $\mathbf{k}$ space $\mathcal{O}_{\Delta\mathbf{k}}(\mathbf{K}',\mathbf{K})$ of this shifted cell $\mathbf{k}$—which is now centered at $\mathbf{K}-\Delta\mathbf{k}$—with cell $\mathbf{k}$ centered at $\mathbf{K}'$:

$$\mathcal{O}_{\Delta\mathbf{k}}(\mathbf{K}',\mathbf{K})=\int_{V(\mathbf{K}')}d\mathbf{k}'\int_{V(\mathbf{K}-\Delta\mathbf{k})}d\mathbf{k}\delta(\mathbf{k}-\mathbf{k}')$$
$$=\int_{V(\mathbf{K})}d\mathbf{k}\int_{V(\mathbf{K}')}d\mathbf{k}'\delta(\mathbf{k}-\mathbf{k}'-\Delta\mathbf{k})\ . \tag{2.20}$$

The evaluation of these geometrical overlap factors is also exemplified in the Appendix. Again replacing $f(\mathbf{x},\mathbf{k};t)$ by its cell average within one phase space cell, we can carry out the spatial integration in Eq. (2.19) and obtain

$$\Delta_k N(\mathbf{R},\mathbf{K};t)=\frac{V(\mathbf{R})}{(2\pi)^3}\sum_{\mathbf{K}'}\mathcal{O}_{\Delta\mathbf{k}}(\mathbf{K}',\mathbf{K})f(\mathbf{R},\mathbf{K}';t)$$
$$-N(\mathbf{R},\mathbf{K};t)\ . \tag{2.21}$$

Now, we use the geometrical relations

$$\mathcal{O}_{\Delta\mathbf{k}}(\mathbf{K},\mathbf{K})=V(\mathbf{K})-\sum_{\mathbf{K}'\neq\mathbf{K}}\mathcal{O}_{\Delta\mathbf{k}}(\mathbf{K}',\mathbf{K})\ ,$$
$$\sum_{\mathbf{K}'\neq\mathbf{K}}\mathcal{O}_{\Delta\mathbf{k}}(\mathbf{K}',\mathbf{K})=\sum_{\mathbf{K}'\neq\mathbf{K}}\mathcal{O}_{\Delta\mathbf{k}}(\mathbf{K},\mathbf{K}')\ , \tag{2.22}$$

and obtain

$$\Delta_k N(\mathbf{R},\mathbf{K};t)=\frac{V(\mathbf{R})}{(2\pi)^3}\sum_{\mathbf{K}'\neq\mathbf{K}}\mathcal{O}_{\Delta\mathbf{k}}(\mathbf{K}',\mathbf{K})f(\mathbf{R},\mathbf{K}';t)$$
$$-\frac{V(\mathbf{R})}{(2\pi)^3}\sum_{\mathbf{K}'\neq\mathbf{K}}\mathcal{O}_{\Delta\mathbf{k}}(\mathbf{K}',\mathbf{K})f(\mathbf{R},\mathbf{K};t)$$
$$=\sum_{\mathbf{K}'\neq\mathbf{K}}\left[\frac{\mathcal{O}_{\Delta\mathbf{k}}(\mathbf{K}',\mathbf{K})}{V(\mathbf{K}')}N(\mathbf{R},\mathbf{K}';t)-\frac{\mathcal{O}_{\Delta\mathbf{k}}(\mathbf{K},\mathbf{K}')}{V(\mathbf{K})}N(\mathbf{R},\mathbf{K};t)\right]\ . \tag{2.23}$$

This equation already resembles Eq. (2.14) and suggests a probabilistic treatment of the acceleration by the external field $\mathbf{E}(\mathbf{R})$ where the normalized overlap factors $\mathcal{O}_{\Delta\mathbf{k}}/V$ play the role of effective scattering probabilities.

Implicitly, Eq. (2.23) requires an extremely fine discretization of $\mathbf{K}$ space in order to guarantee that all particles in a given momentum space cell are accelerated in accordance with the equations of motion, Eq. (2.4). Actually, one can easily verify that Eq. (2.23) always yields the correct mean acceleration in $\mathbf{k}$ space for a periodic $\mathbf{K}$ lattice in the sense that

$$\frac{1}{\Delta t}\sum_{\mathbf{K}}(\mathbf{K}-\mathbf{K}')\frac{\mathcal{O}_{\Delta\mathbf{k}}(\mathbf{K}',\mathbf{K})}{V(\mathbf{K}')}=\frac{\Delta\mathbf{k}}{\Delta t}\ , \tag{2.24}$$

but the fluctuations, given by

$$\sum_{\mathbf{K}}(\mathbf{K}-\mathbf{K}'-\Delta\mathbf{k})^2\frac{\mathcal{O}_{\Delta\mathbf{k}}(\mathbf{K}',\mathbf{K})}{V(\mathbf{K}')}\ , \tag{2.25}$$

vanish identically only when the shift $\Delta\mathbf{k}$ in one time step moves the cell $\mathbf{K}$ exactly on top of another cell $\mathbf{K}''$, i.e.,

$$\mathcal{O}_{\Delta\mathbf{k}}(\mathbf{K}',\mathbf{K})=\delta(\mathbf{K}''-\mathbf{K},\Delta\mathbf{k})$$

for all $\mathbf{K}'$. If, in contrast, the equations of motion yield a change of the wave vector $\Delta\mathbf{k}$ in one time step, which is much smaller than the grid size $\Delta\mathbf{K}$ in $\mathbf{K}$ space, Eq. (2.20) leads to many small and nonzero geometrical overlaps with the neighboring $\mathbf{K}$-space cells. This leads to artificially diffuse accelerations into directions other than the field direction.

Fortunately, Eq. (2.23) can be converted into a form that allows one to use relatively coarse grids and simultaneously suppresses the fluctuations. It follows from Eqs. (2.17) and (2.23) that $\Delta N(\mathbf{R},\mathbf{K};t)_E$ only depends on the ratios $\mathcal{O}_{\Delta\mathbf{k}}/\Delta k$. In addition, Eq. (2.24) guarantees that the equality

$$\sum_{\mathbf{K}}(\mathbf{K}-\mathbf{K}')\frac{\mathcal{O}_{\Delta\mathbf{k}}(\mathbf{K}',\mathbf{K})}{\Delta k V(\mathbf{K}')}=\sum_{\mathbf{K}}(\mathbf{K}-\mathbf{K}')\frac{\mathcal{O}_{\Delta\tilde{\mathbf{k}}}(\mathbf{K}',\mathbf{K})}{\Delta\tilde{k}V(\mathbf{K}')} \tag{2.26}$$

holds for any $\Delta\tilde{\mathbf{k}}$ for a periodic $\mathbf{K}$ lattice. These observations give one the freedom to choose a larger acceleration per time step than the true acceleration $\Delta\mathbf{k}/\Delta t$ but to assign a correspondingly smaller probability to this process. Importantly, by choosing $\Delta\tilde{\mathbf{k}}\gtrsim\Delta\mathbf{K}$ one can guarantee that the overlap factors $\mathcal{O}_{\Delta\mathbf{k}}/\Delta k$ are of the order of unity. In this way, the equations of motion are still preserved in the ensemble average while, at the same time, fluctuations are kept small.

A natural choice for $\Delta\tilde{\mathbf{k}}$ is the mean first-order change in $\mathbf{k}$ during the electron's free flight, which is given by

$$\Delta\tilde{\mathbf{k}}=-\frac{e}{\hbar}\mathbf{E}\tau_{\text{free}}(\mathbf{R},\mathbf{K}) . \tag{2.27}$$

Here, τ_{free} is the mean time of free flight in the phase-space cell $(\mathbf{R},\mathbf{K})$

$$\begin{aligned}\tau_{\text{free}}(\mathbf{R},\mathbf{K})&=\frac{1}{\Gamma(\mathbf{R},\mathbf{K})} ,\\ \Gamma(\mathbf{R},\mathbf{K})&=\frac{1}{\Delta t}\sum_{\mathbf{K}'}P_{\text{coll}}(\mathbf{R},\mathbf{K},\mathbf{K}') .\end{aligned} \tag{2.28}$$

With this modification of Eq. (2.23), the field-induced change in the cell occupation can finally be written as

$$\begin{aligned}\Delta N(\mathbf{R},\mathbf{K};t)_E=\sum_{\mathbf{K}'\neq\mathbf{K}}\{&P_E(\mathbf{R},\mathbf{K}',\mathbf{K})N(\mathbf{R},\mathbf{K}';t)\\&-P_E(\mathbf{R},\mathbf{K},\mathbf{K}')N(\mathbf{R},\mathbf{K};t)\} ,\end{aligned} \tag{2.29}$$

$$\begin{aligned}P_E(\mathbf{R},\mathbf{K}',\mathbf{K})&=\frac{e|\mathbf{E}(\mathbf{R})|\Delta t}{\hbar\Delta\tilde{k}}\frac{\mathcal{O}_{\Delta\tilde{\mathbf{k}}}(\mathbf{K}',\mathbf{K})}{V(\mathbf{K}')}\\&=\frac{\Delta t}{\tau_{\text{free}}(\mathbf{R},\mathbf{K}')}\frac{\mathcal{O}_{\Delta\tilde{\mathbf{k}}}(\mathbf{K}',\mathbf{K})}{V(\mathbf{K}')} ,\end{aligned} \tag{2.30}$$

which has exactly the same form as the collision term Eq. (2.14). The acceleration by the electric field has now been converted to the effective scattering probability P_E. We note that the choice of $\Delta\tilde{\mathbf{k}}$ in Eq. (2.27), together with Eqs. (2.16) and (2.28), is consistent with P_E, representing a properly normalized probability

$$\sum_{\mathbf{K}\neq\mathbf{K}'}P_E(\mathbf{R},\mathbf{K}',\mathbf{K})\leq 1 . \tag{2.31}$$

Finally, we turn to the diffusion-related spatial derivative $\Delta N(\mathbf{R},\mathbf{K};t)_T$ in Eq. (2.13). Employing the same procedure that led to Eq. (2.23), but interchanging the role of position and momentum space, one obtains

$$\begin{aligned}\Delta_T N(\mathbf{R},\mathbf{K};t)=\sum_{\mathbf{R}'\neq\mathbf{R}}\{&P_T(\mathbf{R}',\mathbf{R},\mathbf{K})N(\mathbf{R}',\mathbf{K};t)\\&-P_T(\mathbf{R},\mathbf{R}',\mathbf{K})N(\mathbf{R},\mathbf{K};t)\} .\end{aligned} \tag{2.32}$$

This equation implies that the translation of electrons in real space can also be represented as a scattering process on the microscopic scale of the lattice gas, with P_T playing the role of a hopping probability for the carriers. It is given by

$$P_T(\mathbf{R}',\mathbf{R},\mathbf{K})=\frac{\Delta t}{t_{\Delta x}(\mathbf{K})}\frac{\mathcal{O}_{\Delta\mathbf{x}}(\mathbf{R}',\mathbf{R})}{V(\mathbf{R}')} . \tag{2.33}$$

Equation (2.32) is still nonlocal in position space, since $\Delta\mathbf{x}$ in Eq. (2.33) is determined by Eq. (2.4), and $\mathbf{R}$ and $\mathbf{R}'$ will—for any fixed discretization—generally not be nearest neighbors.

Since, however, the probability Eq. (2.33) depends only on the ratio $\mathcal{O}_{\Delta\mathbf{x}}(\mathbf{R}',\mathbf{R})/\Delta x$, we can use the same arguments that led from Eq. (2.23) to Eqs. (2.29) and (2.30) and choose $\Delta\mathbf{x}$ in Eq. (2.33) in such a way that the equations of motion are still obeyed in the ensemble average but transitions from $\mathbf{R}$ to $\mathbf{R}'$ can occur only between nearest neighbors. An appropriate choice for $\Delta\mathbf{x}$ is $|\Delta\mathbf{x}|=d$, where d is the local nearest-neighbor distance. Importantly, this choice gives overlap factors $\mathcal{O}_{\Delta\mathbf{x}}/V$ equal to unity for nearest neighbors and zero otherwise, guaranteeing that the fluctuations vanish:

$$\sum_{\mathbf{R}}(\mathbf{R}-\mathbf{R}'-\Delta\mathbf{x})^2\frac{\mathcal{O}_{\Delta\mathbf{x}}(\mathbf{R}',\mathbf{R})}{V(\mathbf{R}')}=0 . \tag{2.34}$$

The hopping probability Eq. (2.33) can now be written in a physically transparent form

$$P_T(\mathbf{R}',\mathbf{R},\mathbf{K})=\frac{v(\mathbf{K})}{c}\delta\left[\mathbf{R}-\mathbf{R}',d\frac{\mathbf{K}}{|\mathbf{K}|}\right] , \tag{2.35}$$

where Eq. (2.9) has been used and

$$v(\mathbf{K})=\frac{1}{\hbar}|\nabla_{\mathbf{k}}\varepsilon(\mathbf{K})| \tag{2.36}$$

is the particle's velocity. Here, $c=d/\Delta t$ is the so-called speed of light of the cellular automaton, i.e., the maximum particle velocity. The mesh size in position space needs to be chosen in such a way that $c\geq v$ for all physically relevant velocities.

Equations (2.32) and (2.35) suggest the following physical interpretation. In each time step, the lattice particles hop to one of the neighboring lattice sites in one of the $\mathbf{K}$ directions with probability P_T, and therefore move with the average velocity $v(\mathbf{K})$, in accordance with the equa-

tions of motion.

It is interesting to note that in the area of magnetohydrodynamics, deterministic lattice Boltzmann models have been developed[12,13] recently that lead to equations that are conceptually similar to Eq. (2.32).

The solution of the discretized Boltzmann equation derived above is the cell occupancy $N(\mathbf{R},\mathbf{K};t)$, which is still a continuous variable. We now define Boolean phase-space cell occupancies $n(\mathbf{R},\mathbf{K};t)$ and scattering rates $p=\{0,1\}$ in such a way that the average over an ensemble of CA states—in practice, the average over a large number of cells—yields the continuous macroscopic quantities,

$$\begin{aligned}
&\langle n(\mathbf{R},\mathbf{K};t)\rangle_{\mathrm{CA}}=N(\mathbf{R},\mathbf{K};t)\ ,\\
&\langle p_{\mathrm{coll}}(\mathbf{R},\mathbf{K},\mathbf{K}')\rangle_{\mathrm{CA}}=P_{\mathrm{coll}}(\mathbf{R},\mathbf{K},\mathbf{K}')\ ,\\
&\langle p_E(\mathbf{R},\mathbf{K},\mathbf{K}')\rangle_{\mathrm{CA}}=P_E(\mathbf{R},\mathbf{K},\mathbf{K}')\ ,\\
&\langle p_T(\mathbf{R},\mathbf{R}',\mathbf{K})\rangle_{\mathrm{CA}}=P_T(\mathbf{R},\mathbf{R}',\mathbf{K})\ .
\end{aligned} \tag{2.37}$$

Note that $p_T(\mathbf{R},\mathbf{R}',\mathbf{K})=0$ or $p_T(\mathbf{R},\mathbf{R}',\mathbf{K})=1$ means that a particle either remains at its site $\mathbf{R}$ [with probability $1-v(\mathbf{K})/c$] or hops to its nearest neighbor in direction $\mathbf{K}/|\mathbf{K}|$ with speed c [with probability $v(\mathbf{K})/c$] in a single time step. Collecting all terms, we finally obtain the master equation for the discrete lattice gas

$$\begin{aligned}
n(\mathbf{R},\mathbf{K};t+\Delta t)=n(\mathbf{R},\mathbf{K};t)&+\sum_{\mathbf{R}'=\mathbf{R}_{\mathrm{NN}}}\{p_T(\mathbf{R}',\mathbf{R},\mathbf{K})n(\mathbf{R}',\mathbf{K};t)-p_T(\mathbf{R},\mathbf{R}',\mathbf{K})n(\mathbf{R},\mathbf{K};t)\}\\
&+\sum_{\mathbf{K}'}\{[p_E(\mathbf{R},\mathbf{K}',\mathbf{K})+p_{\mathrm{coll}}(\mathbf{R},\mathbf{K}',\mathbf{K})]n(\mathbf{R},\mathbf{K}';t)\\
&\quad-[p_E(\mathbf{R},\mathbf{K},\mathbf{K}')+p_{\mathrm{coll}}(\mathbf{R},\mathbf{K},\mathbf{K}')]n(\mathbf{R},\mathbf{K};t)\}\ .
\end{aligned} \tag{2.38}$$

The main difference between this result and standard finite-difference schemes is the effective decoupling of position and momentum space, which we arrived at by replacing the kinematic terms in the Boltzmann equation by suitably chosen effective scattering rates. The simple structure of this master equation, which already incorporates the kinematic terms in the Boltzmann equation, allows its solution in parallel on all lattice sites.

III. THE CELLULAR-AUTOMATON TECHNIQUE

A. Principles of the method

In this section we discuss the general steps one needs to carry out in order to solve the Boltzmann equation in the cellular-automaton form, Eq. (2.38). First, we point out that CA contain two length scales. The fictitious lattice-gas particles move on a microscale, whereas the physical-particle trajectories and other observables are computed on a coarser scale, the macroscale. Criteria for the choice of lattice-mesh sizes and examples are discussed in subsequent sections.

A cellular-automaton simulation can be carried out in two ways, either in a particle representation or in a site representation. In the first case, one follows the trajectory of each particle individually in phase space and updates its phase-space location after every time step. In the second case, one considers the site occupancies in phase space as primary variables and increases or decreases them after each scattering event.

If the occupation of phase space is very sparse, the particle representation is more efficient, since the computer time is proportional to the number of particles instead of being proportional to the number of phase-space cells. This situation will prevail for low doping concentrations. We show here schematically the procedure for a CA simulation in the particle representation.

(1) Choose a time step, mesh size, and lattice size in $\mathbf{R}$ space and $\mathbf{K}$ space on the microscale. Define blocks of lattice points forming the macroscale.

(2) For each initial state $(\mathbf{R},\mathbf{K})$, set up three scattering tables containing all final states with a frequency proportional to the probabilities $P_{\mathrm{coll}}(\mathbf{R},\mathbf{K},\mathbf{K}')$, $P_E(\mathbf{R},\mathbf{K},\mathbf{K}')$, and $P_T(\mathbf{R},\mathbf{R}',\mathbf{K})$, respectively, utilizing symmetry. In addition, set up nearest-neighbor tables that reflect the topology of the lattice in position space.

(3) Initialize the particle distribution and assign $(\mathbf{R},\mathbf{K})$ to each of the particles $i=1,\ldots,N$.

(4) Consider particle $i=1,\ldots,N$.

(5) Local $\mathbf{k}$-space scattering step at site $\mathbf{R}$: Use the local scattering table for quantum-mechanical collisions (P_{coll}) and pick out randomly the final $\mathbf{k}$ state; transfer particle i from state $(\mathbf{R},\mathbf{K})\rightarrow(\mathbf{R},\mathbf{K}')$; use the local scattering table for the $\mathbf{k}$-space acceleration due to the local electric field $\mathbf{E}(\mathbf{R})$ (P_E) and pick out randomly the final $\mathbf{k}$ state; transfer particle i from state $(\mathbf{R},\mathbf{K})\rightarrow(\mathbf{R},\mathbf{K}')$.

(6) Translation step for state $\mathbf{K}'$: Use the local scattering table for the motion in real space (P_T) and pick out randomly the final cell $\mathbf{R}'$; transfer particle i from state $(\mathbf{R},\mathbf{K}')\rightarrow(\mathbf{R}',\mathbf{K}')$, with $\mathbf{R}'=\mathbf{R}$ or $\mathbf{R}'=\mathbf{R}_{\mathrm{NN}}$, where $\mathbf{R}_{\mathrm{NN}}$ denotes the neighbor of cell $\mathbf{R}$ in the direction of $\mathbf{K}'$.

(7) Repeat steps (5) and (6) for all particles.

(8) Determine particle number $N(\mathbf{R},\mathbf{K})$ on macroscale and solve Poisson's equation for the electric field $\mathbf{E}(\mathbf{R})$.

Steps (4)–(7) or (4)–(8) represent one time step.

The cellular-automaton method developed in this paper is most useful for transport properties that are difficult or very time consuming to predict accurately with alternative methods, such as the distribution function for strongly inhomogeneous charge distributions or for very high carrier concentrations.[18]

In this situation, it is more efficient to invoke the site representation and loop over phase space-cell occupancies instead of following individual particles. The site representation is closer to the original concept of CA and offers the following advantages.

(i) The local distribution function on any given site is known at all times without the need to scan all particles. This is particularly efficient for scattering kernels that depend on the local distribution of carriers, such as for degenerate electron systems, impact ionization of trapped carriers, and carrier-carrier interactions. Due to the small number of **K** states attached to each cell **R** on the microscale, complete two-particle scattering tables for the short-range part of the electron-electron interaction can be set up and stored as look-up tables. The observation of Pauli's principle is also straightforward, since $f(\mathbf{K})$ is the primary variable in the cellular-automaton algorithm.

(ii) The distribution functions in spatially separate regions develop in time according to their own local scattering tables and there is no need to share these tables globally. This is the key advantage of the method if several or many parallel processors are available.

(iii) Since the occupancies in single-phase-space cells are small integers, they can be stored bitwise, allowing the study of very large dynamical systems with only moderate storage requirements.

B. Computational details and examples

The examples and applications of the method that are discussed in this paper primarily serve to demonstrate that the CA method is a robust scheme that does not depend critically on the chosen discretization on the microscale of the lattice and easily reaches the accuracy of the standard ensemble Monte Carlo technique. In fact, we purposely choose a rather crude discretization here and only include the standard single-particle scattering mechanisms in the particle representation of the cellular automaton in order to be able to compare to published and reliable Monte Carlo simulations. Additional results with degenerate carriers and impact ionization will be presented in a later publication.

Let us consider high-field transport in a bulk semiconductor with acoustic-phonon, optic-phonon, and ionized-impurity scattering. We assume the carrier distribution to be inhomogeneous only in two dimensions, which is appropriate for planar devices. In this situation, a possible realization of an automaton is a two-dimensional hexagonal **R** lattice with a lattice spacing of the order of 1 nm and a three-dimensional **k** space associated with each site **R**. This **k** space is divided into six segments pointing toward the nearest neighbors in the **R** lattice. These six directions are then the only possible velocity directions on the microscale. Furthermore, each of these six segments is subdivided into shells, corresponding to different magnitudes $|\mathbf{K}|$ or—equivalently—carrier energies. A reasonable choice is to set these energies to multiples of optical-phonon energies $n\hbar\omega$, with n ranging typically from 1 to 30. This fixes the **K** lattice, the energy range, and resolution of the cellular automaton. A schematic picture of a few **K** cells is shown in Fig. 1. In position space, the inclusion of 10^4 to 10^5 **R**-space cells on the microscale proved sufficient for the results presented in Sec. IV. The transformation to the macroscale is accomplished by averaging over blocks of typically 10^2 **R**-space cells.

Steps (5) and (6) in Sec. III A are most efficiently carried out with scattering tables that contain all possible final states with a frequency determined by their respective probabilities. Making use of symmetry, one type of table is required for each initial magnitude of the wave vector in the Brillouin zone $|\mathbf{K}|$ and impurity concentration to represent the total scattering probabilities for the quantum-mechanical processes. An additional type of table is required for each magnitude of the electric field $|\mathbf{E}|$ and each **K** vector. A third set of tables is required for each $|\mathbf{K}|$ to discriminate between the moving and the stopped particles. Only the impurity-related tables are **R** dependent. In a typical simulation, we have used ten discrete values to represent the different impurity concentrations in doping profiles, ten values to represent the magnitude of the electric field $|\mathbf{E}|$, and 30 values for the modulus of the wave vector $|\mathbf{K}|$ in each band, assuming either a parabolic or nonparabolic dispersion. Since there are six different **K** directions in a two-dimensional hexagonal real-space lattice, each of the scattering tables contains 180 final states for electrons in one valley. We found 5×10^3 to 1×10^4 entries in each table to adequately represent the relative probabilities of the final states. The length of these final-state arrays can be reduced by one order of magnitude by separating out the self-scattering

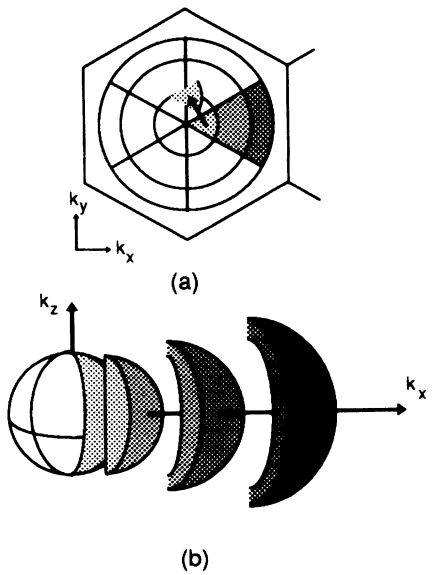

FIG. 1. (a) Top view of a two-dimensional hexagonal cell in real space. Also shown are the three-dimensional **k** cells associated with it. In this figure, only 18 **k** cells (six **k** directions and three **k** moduli) are shown. Within a time step, each cell moves by a vector $\Delta\mathbf{k}$. This is shown schematically for one of the inner **k** cells. The shifted cell overlaps with several other **k** cells. (b) Three-dimensional side view of the **k** cells that correspond to the hatched cells in (a).

events where the initial and final states are identical. In summary, the storage requirement for all scattering tables together is approximately 2×10^6 short integers (bytes, where 1 byte equals 8 bits). In a simulation that treats the **k** space fully three dimensionally it is approximately twice as much.

In semiclassical transport calculations, the long-range part of the Coulomb interaction between the charge carriers is taken into account by augmenting the Boltzmann equation by the Poisson equation. In the present work, the Poisson equation is solved on the macroscale of the cellular automaton either using direct matrix inversion or one of the standard relaxation methods.[16] These methods are already well adapted to modern vector or parallel processing. In this way, the electric field $\mathbf{E}(\mathbf{R})$ is first determined as a continuous quantity on a block of cells. Subsequently, it is assigned to each individual microcell by decomposing the field into its components along the two closest hexagonal $|\mathbf{K}|$ directions or simply by assigning **E** to the closest hexagonal direction.

The present quasi-two-dimensional treatment of **K** space causes the various **K** cells to differ significantly in size and shape (see Fig. 1). In particular, this structure of the **K** cells causes the electron distribution to acquire a continuously larger spread along the k_z direction when the electric field accelerates the carriers, which leads approximately to a 10% underestimate of the free acceleration of particles by the electric field. We found that this geometrical artifact can be fairly accurately accounted for by (i) increasing the field-related scattering probabilities P_E in Eq. (2.30) by a constant factor of 1.1 for a wide range of fields both for Si and GaAs, and (ii) by a careful choice of the origin of the wave vectors within the **K** cells. This choice enters the calculation of the hopping probabilities in Eq. (2.33) and the ensemble averages of the momentum. We put this origin at the cell average $\langle\mathbf{K}\rangle$ for the six innermost **K** cells, and at the minimum **k** vector in the x-y plane within a cell **K** for all other cells.

It is clear from the foregoing discussion that the usage of a fully three-dimensional cubic or hexagonal close-packed **R** lattice is preferable for realistic simulations, since it avoids the geometrical artifacts of a two-dimensional lattice. In this case, a nearest-neighbor cellular automaton contains 12 velocity directions, giving a significantly better resolution of transport effects in **x** space as well as in **k** space, while requiring only twice as much memory as a two-dimensional cellular automaton. In principle, higher dimensional hypercubes also could be chosen.[12] Nevertheless, the applications of the method presented in Sec. IV are based on two-dimensional hexagonal **R** lattices.

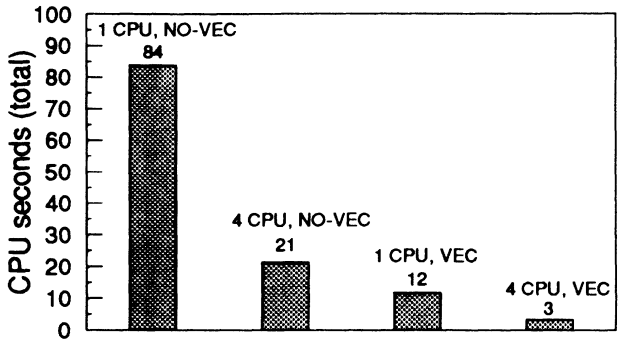

FIG. 2. Comparison of CPU times of the present cellular-automaton simulation for 300 000 lattice particles and 100 time steps on a Cray YMP computer. The results have been obtained either with (VEC) or without (NO-VEC) vectorization and with either a single (1 CPU) or four concurrent (4 CPU) processors. This figure illustrates the high degree of parallelization that can be obtained with the new cellular-automaton method.

C. CA-lattice parameters and limitations

Two basic parameters of a cellular-automaton simulation have not been explicitly specified yet, namely the lattice constant d and the time step Δt. The lattice constant must clearly be small enough to resolve all physically relevant inhomogeneities and the time step must be shorter than any scattering time. However, there are two additional criteria that need to be observed. First, the maximum particle velocity or speed of light $c=d/\Delta t$ of the cellular automaton must be larger than any physically relevant particle velocity. With the choice of $\Delta t=1$ fs and $d=1$ nm, this criterion can easily be obeyed in semiconductors, since $c=10^8$ cm/sec is significantly higher than the saturation velocities in semiconductors.

The second criterion for d and Δt is less obvious and arises from the replacement of the deterministic particle trajectories by probabilistic hoppings in **x** space and **k** space. As pointed out before, the cellular-automaton equation (2.38) only guarantees that the particle trajectories follow the equations of motion in the ensemble average. This leads to a built-in artificial diffusion of the carriers that depends on the lattice parameters.

For the longitudinal diffusion, the situation is analogous to a one-dimensional random-walk problem. Let us consider a particle that either hops by a distance d within a time step Δt or does not move. When the hopping probability is γ, the particle has an average velocity $v=\gamma d/\Delta t$. But the probabilistic nature of the motion also yields a longitudinal diffusion with the diffusion constant D given by

$$D=\frac{d^2}{2\Delta t}\gamma(1-\gamma)\ . \tag{3.1}$$

In addition, an artificial transversal diffusion is introduced by the finite number of nearest-neighbor directions. Let us assume that the electric-field direction lies exactly in between two planar hexagonal lattice vectors and that the particle gets scattered into these directions with equal probability. This situation leads to a diffusion transverse to the applied field with a diffusion constant that turns out to be identical to Eq. (3.1) with $\gamma=0.5$.

Fortunately, with the lattice parameters $\Delta t=1$ fs and $d=1$ nm, Eq. (3.1) gives an artificial diffusion constant of $D<1.3$ cm^2/s, which is small compared with typical diffusion constants in Si or GaAs at room temperature ($\sim0.5\times10^2$ cm^2/s). For very high electric fields, on the other hand, the physical diffusion constants can become small and a careful selection of the CA parameters is

necessary to guarantee that built-in diffusions remain small.

IV. TESTS AND COMPARISONS

Figure 2 illustrates the efficiency of the present CA method by depicting the computer time required for the solution of the CA equations (without the Poisson equation) with 300 000 particles as a function of the number of processors. Even on a moderately parallel system such as a Cray YMP computer with four processors, one gains a factor of 25 in computer time when running the cellular-automaton code concurrently on four processors and switching on the automatic vectorization capabilities of this computer. The computer time scales strictly linearly with the number of processors. We have obtained similar results on several other parallel computer architectures. In order to test the accuracy and usefulness of the present method in realistic applications, we now discuss several comparisons of CA simulations with Monte Carlo and drift-diffusion calculations for n-type Si and GaAs.

A. Homogeneous transport

In Fig. 3, we show the drift velocity in bulk n-type Si as a function of the electric field (along the [111] direction) as calculated with the CA technique and incorporating ionized-impurity and phonon scattering. The phonon scattering rates for Si together with the band-structure parameters are specified in Table I. For comparison, the results of previous ensemble Monte Carlo simulations[19] are also shown. The results demonstrate the capability of the present cellular-automaton model to correctly reproduce both the Ohmic low-field mobility and the high-field transport regime. The agreement with the Monte Carlo results[19] is excellent for the whole range of electric fields.

TABLE I. Material parameters for Si used in the cellular-automata simulations. The values are taken from Ref. 15.

		Si
Longitudinal effective mass m_l^*/m		0.98
Transverse effective mass m_t^*/m		0.19
Nonparabolicity factor α		0.5
Dielectric constant		11.8
Intervalley phonons:		
TA modes: g_1	coupling (eV/cm)	0.5×10^8
	energy (eV)	0.012
TA modes: f_1	coupling (eV/cm)	0.3×10^8
	energy (eV)	0.018
LA modes: g_2	coupling (eV/cm)	0.8×10^8
	energy (eV)	0.0185
LA modes: f_2	coupling (eV/cm)	2.0×10^8
	energy (eV)	0.047
LO mode: g_3	coupling (eV/cm)	11.0×10^8
	energy (eV)	0.062
TO mode: f_3	coupling (eV/cm)	2.0×10^8
	energy (eV)	0.059
Acoustic-deformation potential (eV)		9.0

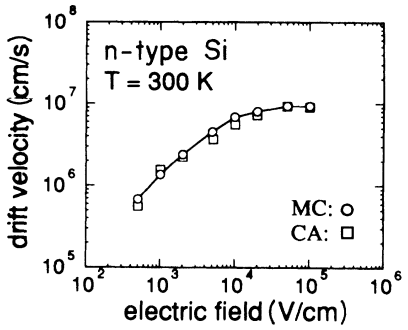

FIG. 3. Theoretical drift velocity in bulk n-type Si as a function of the electric field along the [111] direction. The circles are the Monte Carlo results of Ref. 19 and are interconnected by lines to guide the eye. The squares represent the cellular-automaton results.

The slightly lower drift velocity near electric fields of about 10 kV/cm predicted by the CA model has two causes. First, the scattering rates in Ref. 19 differ somewhat from the ones given in Table I, which contains more recent values. Second, the restricted **k**-space discretization used in this paper leads to a slight overestimation of the diffusive motion as discussed in Sec. III C. This effect can also be noticed in the calculated carrier energy and the longitudinal-diffusion coefficient, shown in Figs. 4 and 5, and accounts for approximately half of the discrepancy between the present calculations and the Monte Carlo results for high fields. Still, the overall agreement between the two methods is very satisfactory and could be further improved by employing fully three-dimensional **x** and **k** lattices.

The velocity overshoot of electrons in GaAs provides another stringent test for any microscopic transport calculation. In Figs. 6 and 7, we compare the CA results with previous Monte Carlo calculations[20,21] for n-type GaAs. The CA simulations use a two-valley model (Γ,L) with parabolic bands and take into account phonon and

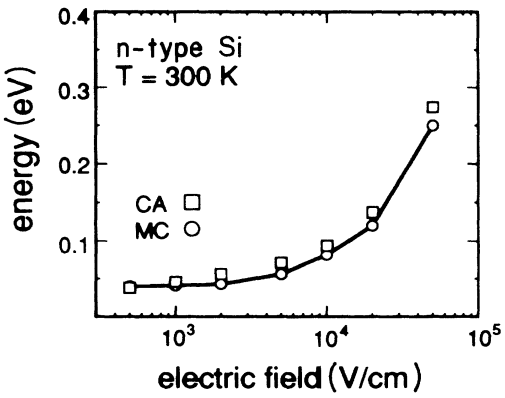

FIG. 4. Kinetic energy of electrons in n-type Si at room temperature as a function of the electric field acting along the [111] direction. The circles are the Monte Carlo results of Ref. 19 and are interconnected by lines to guide the eye. The squares represent the cellular-automaton results.

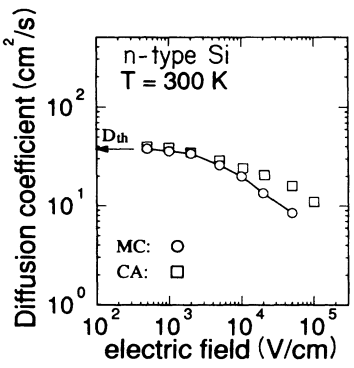

FIG. 5. Field-dependent longitudinal-diffusion coefficient in n-type Si at room temperature. The circles are the Monte Carlo results of Ref. 19 and are interconnected by lines to guide the eye. The squares represent the cellular-automaton results. The thermal diffusivity is indicated by an arrow (Ref. 23).

ionized-impurity scattering. The relevant coupling parameters employed in the calculation are summarized in Table II. The Monte Carlo results, on the other hand, are based on a more accurate three-valley model and nonparabolic bands.[20,21] Nevertheless, the overall agreement between the two methods is again very satisfactory.

These results show that a very crude discretization of momentum space on the microscale of the cellular automaton can already capture the physical transport properties on the macroscale quantitatively. However, these examples do not test the adequacy of the present model for spatially inhomogeneous distribution functions. This is the subject of Sec. IV B.

B. Inhomogeneous transport

In order to test the cellular-automaton method for inhomogeneous systems, simulations for a planar Si metal-semiconductor field-effect transistor (MESFET) have been carried out. The MESFET is characterized by the following data. The source, gate, and drain contacts, as well as the distance between the contacts, are 0.5 μm.

TABLE II. Material parameters for GaAs used in the cellular-automata simulations. The values are taken from Refs. 22 and 23.

	GaAs
Γ-L energy separation (eV)	0.33
Effective mass $(m^*/m)_{\Gamma\ \text{valley}}$	0.0665
Effective mass $(m^*/m)_{L\ \text{valley}}$	0.222
Static dielectric constant ϵ_0	12.9
Optical dielectric constant ϵ_∞	10.9
LO phonon energy (eV)	0.036
Γ-L intervalley coupling (eV/cm)	1.0×10^9
L-L intervalley coupling (eV/cm)	1.0×10^9

The width of the n-doped active layer ($N_D=10^{17}$ cm^{-3}) and of the weakly n-doped substrate ($N_D=10^{15}$ cm^{-3}) is 0.21 μm. The Schottky barrier at the gate is assumed to be 0.8 V. For the cellular automaton, the **x** grid consists of 400×80 lattice sites with a lattice constant of $d=6.25$ nm. 180 **K** cells are attached to each lattice site and the time step is given by $\Delta t=4.5$ fs, corresponding to a maximum velocity of $c=1.8\times10^8$ cm/s.

Figure 8 compares our results for the drain characteristics of the MESFET with realistic drift-diffusion model calculations (Cornell University Program for IC devices, abbreviated as CUPID) of Ref. 24. The drain currents agree very well with one another. The larger drain conductance predicted by the CA simulations, however, is in much better agreement with the experimental[25] value of 74.6 mS/cm than the value obtained by CUPID. The present technique gives approximately 100 mS/cm, whereas CUPID predicts only 16.2 mS/cm. This difference originates in the neglect of the substrate in the CUPID calculation,[24] thereby cutting off the substrate current.

In Fig. 9(a) we compare the average drift velocity v_d and in Fig. 9(b) the electric field parallel to the gate just beneath the gate of the Si MESFET, as obtained by the CA simulation and the CUPID model of Ref. 24, respectively. Both types of calculations predict the calculated electric fields to reach their highest values near the drain

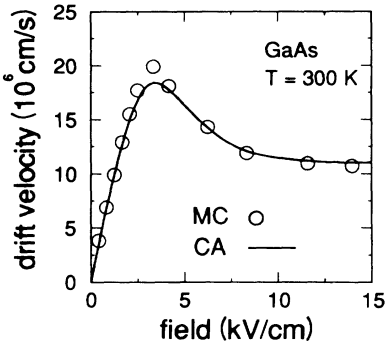

FIG. 6. Theoretical drift velocity in bulk n-type GaAs as a function of the electric field. The full curve has been obtained with the present cellular-automaton method, whereas the circles mark the Monte Carlo results of Ref. 21.

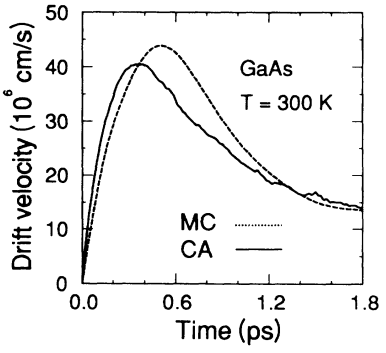

FIG. 7. Time dependence of predicted drift velocity in n-type GaAs with electron concentration $n=10^{17}$ cm^{-3} and electric field $E=10$ kV/cm. The full and dashed curves represent cellular-automaton simulations and ensemble Monte Carlo results from Ref. 20, respectively.

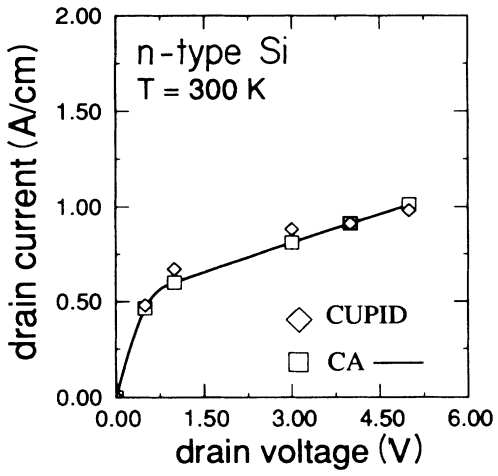

FIG. 8. Drain current vs applied drain voltage for a planar Si MESFET with 0.5-μm gate length, calculated with the cellular-automaton technique (rectangles, connected by lines to guide the eye) and with the device simulator CUPID (Cornell University program for integrated devices, Ref. 24).

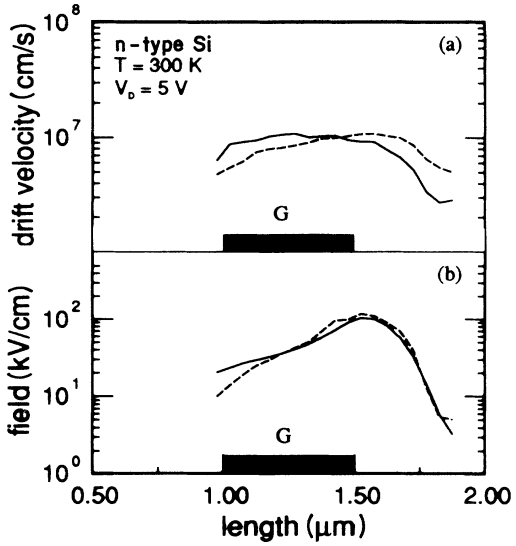

FIG. 9. (a) The longitudinal-drift velocity and (b) the electric field, at 0.175 μm beneath the gate, in a planar Si MESFET with 0.5-μm gate length. The full lines are obtained with the present cellular-automaton technique, whereas the dashed lines have been calculated with the device simulator CUPID (Ref. 24) which is based on the drift-diffusion approximation.

end of the gate region (right-hand side in Fig. 9) and are in excellent agreement with one another. However, the drift-diffusion calculations fail to reproduce the velocity overshoot at the source end of the gate region predicted both by Monte Carlo[20] methods and the cellular-automaton technique. This velocity overshoot can be seen in Fig. 9(a) and, in effect, decouples the maximum in v_d and in the field. We study this effect in more detail in the next section. We conclude that the present cellular-automaton method faithfully reproduces known high-field solutions of the Boltzmann equation in inhomogeneous situations as well as in homogeneous cases.

V. APPLICATIONS

Velocity overshoot in Si MESFET's

Velocity overshoot is a well-studied phenomenon in GaAs, whereas it can become significant in Si only for very small devices. As a simple application of the cellular-automaton method, we study the onset of overshoot effects in the drift velocity of a Si MESFET. The device geometries are the same as in Sec. IV B, except that the contact dimensions are reduced to 0.3 μm.

In Fig. 10(b), we show the calculated longitudinal electric field $E(x_\parallel)$ and in Fig. 10(a) the longitudinal drift velocity $\langle v_d(x_\parallel)\rangle$ beneath the gate. We have averaged the drift velocity over the active region according to the equation

$$\langle v_d(x_\parallel)\rangle = \frac{\int^{\text{active layer}} dx_\perp v_d(x_\parallel,x_\perp) n(x_\parallel,x_\perp)}{\int dx_\perp n(x_\parallel,x_\perp)} . \quad (5.1)$$

The results in Fig. 10 are shown for three different drain voltages, namely 1, 3, and 5 V. Only for the lowest voltage, v_d and E are proportional to each other in the whole gate region, as one expects from a drift-diffusion picture. The electric field increases along the gate region, peaks near the end of the gate, and drops rapidly toward the drain contact (right-hand side of Fig. 10). One can see that the peak of the electric field shifts towards the drain for higher voltages due to the higher depletion of carriers

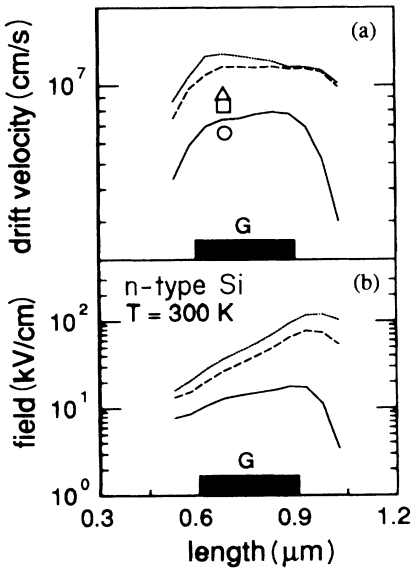

FIG. 10. (a) The longitudinal-drift velocity and (b) the electric field under the gate for a Si MESFET, obtained with the present CA method. The full, dashed, and dotted lines correspond to drain voltages of 1, 3, and 5 V, respectively. The gate voltage is 0 V. The symbols in the upper curve indicate bulk saturation drift velocities for the same electric fields, whereas the circle, square, and triangle correspond to the drain voltages of 1, 3, and 5 V, respectively.

at the drain end of the gate (pinch-off). Even for the smallest voltage of 1 V, v_d becomes slightly higher than the homogeneous bulk-drift velocity near the source end of the gate [left-hand side of Fig. 10(a)], indicating a small overshoot. The circle, square, and triangle in Fig. 10(a) correspond to 1, 3, and 5 V, respectively, and show the stationary-drift velocity in bulk Si for an electric field equal to the field shown in Fig. 10(b) at 0.7 μm. For 3 and 5 V, the overshoot is more pronounced. In Si, this quasiballistic transport can occur only in a small portion of the gate region near the source end, since the saturation value of the velocity is reached in about 0.5 ps, which corresponds to 0.05 μm for $v_d = 10^7$ cm/s.[16] As a consequence, the drift velocity reaches saturation velocity at the drain end of the gate for both 3 and 5 V drain voltage (see Fig. 10).

VI. CONCLUSIONS

In this paper we have developed a method of solving the semiclassical Boltzmann transport equation for the distribution function $f(\mathbf{x},\mathbf{k};t)$. It was shown that the Boltzmann equation can be transformed to a Boolean master equation, which constitutes a nearest-neighbor cellular automaton in real space. This effectively decouples $\mathbf{x}$ and $\mathbf{k}$ space. In Sec. III, a concrete cellular-automaton algorithm was developed which is highly suited for modern computer hardware and allows an efficient treatment of complex scattering kernels and geometries. The applications and examples have shown that this technique is robust and works well even for coarse discretizations. We believe that this technique can be useful for transport phenomena in different areas of physics, particularly for strongly inhomogeneous and anisotropic systems that are determined by an interplay of external driving forces and diffusion.

ACKNOWLEDGMENTS

Numerous helpful discussions with P. Lugli, E. Gornik, and K. Hoffmann are gratefully acknowledged. We also thank Dr. Steinhöfer from the Leibnitz Rechenzentrum München for benchmarking our codes on the Cray YMP computer. This work is supported by the Deutsche Forschungsgemeinschaft and by Siemens Corporation.

APPENDIX: CALCULATION OF CELL-AVERAGED SCATTERING PROBABILITIES

In this Appendix, we exemplify the calculation of the cellular-automaton scattering rules for the case of emission of nonpolar optical phonons. In this case, the quantum-mechanical scattering rate is independent of the position $\mathbf{R}$ and is given by

$$w_{\text{ph-em}}(\mathbf{k},\mathbf{k}') = \frac{\pi (D_t K)^2}{\rho V \omega_{\text{op}}} (N_{\text{op}}+1)\delta(\varepsilon(\mathbf{k}')-\varepsilon(\mathbf{k})+\hbar\omega_{\text{op}}) , \tag{A1}$$

where N_{op} is the occupation number, $\hbar\omega_{\text{op}}$ is the optical-phonon energy, $D_t K$ is the deformation-potential coupling constant, and ρ is the mass density. First, we integrate this expression over the final-state cell $\mathbf{K}'$ and define

$$\begin{aligned} w(\mathbf{k},\mathbf{K}') &= V \int_{V(\mathbf{K}')} \frac{d\mathbf{k}'}{(2\pi)^3} w_{\text{ph-em}}(\mathbf{k},\mathbf{k}') \\ &= \frac{(D_t K)^2}{8\pi^2 \rho \omega_{\text{op}}} (N_{\text{op}}+1) \int_0^{\pi/3} \int_0^{\pi} \int_{k_l'}^{k_u'} k'^2 d\phi' \sin\Theta' d\Theta' dk' \delta(\varepsilon(\mathbf{k}')-\varepsilon(\mathbf{k})+\hbar\omega_{\text{op}}) \\ &= \frac{(D_t K)^2 m^*}{12\pi\rho\omega_{\text{op}}\hbar^2} (N_{\text{op}}+1) \sqrt{\mathbf{k}^2-\mathbf{k}_{\text{op}}^2} . \end{aligned} \tag{A2}$$

Here, k_l' and k_u' are the lower and upper bounds of the wave vector $\mathbf{k}'$ in polar coordinates; $\mathbf{k}'=(\phi',\Theta',k')\in\mathbf{K}'$ and a parabolic electron mass m^* was used for $k_{\text{op}}^2=(2m^*\omega_{\text{op}})/\hbar^2$. We can now integrate over the initial-state cell and obtain

$$\begin{aligned} P_{\text{ph-em}}(\mathbf{K},\mathbf{K}') = &\frac{(D_t K)^2 m^*}{18\pi\rho\omega_{\text{op}}\hbar^2} (N_{\text{op}}+1) \frac{\Delta t}{V(\mathbf{K})} \\ &\times \int_{k_l}^{k_u} dk\, k^2 \sqrt{k^2-k_{\text{op}}^2} . \end{aligned} \tag{A3}$$

For the calculation of the field scattering rates, let the $\mathbf{k}$ vector in the initial cell $\mathbf{K}$ be $\mathbf{k}=(\phi,\Theta,k)$. The shift $\Delta\mathbf{k}$ in $\mathbf{k}$ space due to the electric field is given by Eq. (2.27) and gives a final $\mathbf{k}$ vector $\mathbf{k}'=(\phi',\Theta',k')$, where

$$\begin{aligned} k' &= \sqrt{k^2-\Delta k^2-2k\sin\Theta(\Delta k_x\cos\phi+\Delta k_y\sin\phi)} , \\ \phi' &= \arctan\left[\frac{k\sin\phi\sin\Theta-\Delta k_y}{k\cos\phi\sin\Theta-\Delta k_x}\right] , \\ \Theta' &= \arccos\left[\frac{k\cos\Theta}{k'}\right] . \end{aligned} \tag{A4}$$

The overlap functions $O_{\Delta\mathbf{k}}(\mathbf{K},\mathbf{K}')$ are then calculated by dividing the cell $\mathbf{K}$ into many small cells, shifting these small cells by $\Delta\mathbf{k}$ and determining the final cell $\mathbf{K}'$. All contributions that lie within the cell $\mathbf{K}'$ are then added.

[1]For recent reviews, see *Lattice Gas Methods for PDE's: Theory, Application, and Hardware,* edited by G. D. Doolen [Physica D **45**, 1 (1990)].

[2]See articles in *Cellular Automata and Modeling of Complex Physical Systems,* edited by P. Manneville, N. Boccara, G. Y. Vichniac, and R. Bideaux (Springer, Berlin, 1989).

[3]U. Frisch, B. Hasslacher, and Y. Pomeau, Phys. Rev. Lett. **56**, 1505 (1986).

[4]U. Frisch, D. d'Humières, B. Hasslacher, P. Lallemand, Y. Pomeau, and J. P. Rivet, Complex Systems **1**, 649 (1987).

[5]D. Dab, J.-P. Boon, and Y.-X. Li, Phys. Rev. Lett. **66**, 2535 (1991).

[6]R. Kapral, A. Lawniczak, and P. Masiar, Phys. Rev. Lett. **66**, 2539 (1991).

[7]Y. Bar-Yam, D. Kandel, and E. Domany, Phys. Rev. B **41**, 12 869 (1990).

[8]J. von Neumann, *Theory of Self-Reproducing Automata* (University of Illinois Press, Chicago, 1966).

[9]S. Chen, K. Diemer, G. D. Doolen, K. G. Eggert, and B. J. Travis, Physica D **47**, 72 (1991).

[10]J. A. Somers and P. C. Rem, in *Cellular Automata and Modeling of Complex Physical Systems* (Ref. 2), p. 161.

[11]K. Molvig, P. Donis, R. Miller, J. Myczkowski, and G. Vichniac, in *Cellular Automata and Modeling of Complex Physical Systems* (Ref. 2), p. 206.

[12]S. Chen, H. Chen, D. Martinez, and W. Matthaeus, Phys. Rev. Lett. **67**, 3776 (1991).

[13]L.-S. Luo, H. Chen, S. Chen, G. D. Doolen, and Y. C. Lee, Phys. Rev. A **43**, 7097 (1991).

[14]W. Fawcett, A. D. Boardman, and S. Swain, J. Phys. Chem. Solids **31**, 1963 (1970).

[15]C. Jacoboni and L. Reggiani, Rev. Mod. Phys. **55**, 645 (1986).

[16]C. Jacoboni and P. Lugli, *The Monte Carlo Method for Semiconductor Device Simulation* (Springer, Vienna, 1989).

[17]K. Kometer, G. Zandler, and P. Vogl, Semicond. Sci. Technol. **7**, B154 (1992).

[18]M. Fischetti, Phys. Rev. B **38**, 9721 (1988).

[19]C. Canali, C. Jacoboni, G. Ottaviani, A. Alberigi-Quaranta, Appl. Phys. Lett. **27**, 278 (1975).

[20]A. Yoshii, M. Tomizawa, and K. Yokoyama, IEEE Trans. Electron Devices **ED-30**, 1376 (1983).

[21]J. Pozela and A. Reklaitis, Solid State Commun. **27**, 1073 (1978).

[22]M. A. Osman and D. K. Ferry, Phys. Rev. B **36**, 6018 (1987).

[23]G. Harbeke, O. Madelung, and U. Rössler, in *Tables Numerical Data and Functional Relationships in Science and Technology,* edited by O. Madelung, M. Schulz, and H. Weiss, Landolt-Börnstein, New Series, Group III, Vol. 17, Pt. a (Springer, Heidelberg, 1982).

[24]T. Wada and J. Frey, IEEE Trans. Electron Devices **ED-26**, 476 (1979).

[25]W. Baechtold *et al.*, Electron. Lett. **9**, 232 (1973).

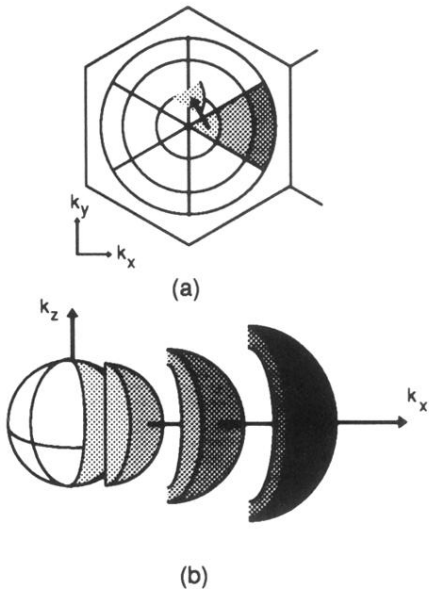

FIG. 1. (a) Top view of a two-dimensional hexagonal cell in real space. Also shown are the three-dimensional **k** cells associated with it. In this figure, only 18 **k** cells (six **k** directions and three **k** moduli) are shown. Within a time step, each cell moves by a vector $\Delta\mathbf{k}$. This is shown schematically for one of the inner **k** cells. The shifted cell overlaps with several other **k** cells. (b) Three-dimensional side view of the **k** cells that correspond to the hatched cells in (a).

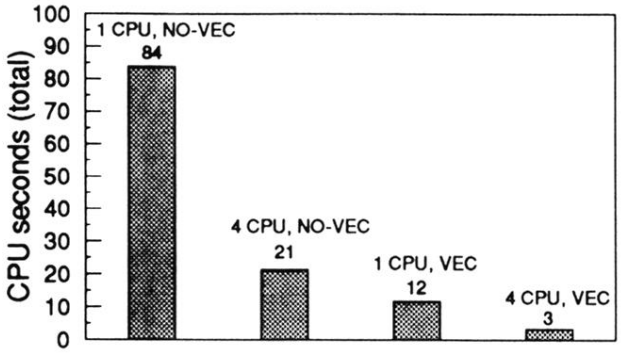

FIG. 2. Comparison of CPU times of the present cellular-automaton simulation for 300 000 lattice particles and 100 time steps on a Cray YMP computer. The results have been obtained either with (VEC) or without (NO-VEC) vectorization and with either a single (1 CPU) or four concurrent (4 CPU) processors. This figure illustrates the high degree of parallelization that can be obtained with the new cellular-automaton method.